LUMINESCENT $CuInSe_2$–BASED CORE/SHELL NANOCRYSTALS: CHARACTERIZING DEFECTS IN $CuInSe_2$ NANOCRYSTALS

Soa-Jin Catherine Sher

CHE 679H
Engineering Honors Program
Plan II Honors Program
The University of Texas at Austin

May 2015

Brian A. Korgel, Ph.D.

Department of Chemical Engineering

Supervising Professor

D'Arcy Randall, Ph.D.

Department of Chemical Engineering

Second Reader

Abstract

Author: Soa-Jin Catherine Sher

Title: Luminescent CuInSe2–Based Core/Shell Nanocrystals: Characterizing Defects in CuInSe2 Nanocrystals

Supervising Professor: Brian Korgel, Ph.D.

As interest continues to grow in new materials for next-generation photovoltaic (PV) devices (i.e. solar cells), it is important to understand the mechanisms and limitations of promising materials. Many researchers are focused on the use of semiconductor nanocrystals (NCs) in PV devices because of their potential to be deposited in thin films via solution, which is more cost-effective than traditional methods. This study focuses on CuInSe2 (CISe) NCs, which are part of a larger class of materials known as CuInxGa1-xSe2 (CIGS). CIGS is well-known in the PV industry, especially for its use on flexible substrate materials, which have significant cost and processing advantages over traditional, bulky, glass-based solar cells. However, defects within or on the surface of the CIGS NCs limit the movement of holes and electrons, affecting the ability of the NCs to extract charge carriers; these defects ultimately result in lower-efficiency PV devices. The purpose of this study is to better understand the defects within CISe NCs by coating them with ZnS shells. A Zn-based shell was successfully formed around a CISe NC without compromising the integrity of the CISe NC. The shell also successfully passivated the surface defects and increased the efficiency of the CISe NCs. By creating luminescent CISe-based core/shell NCs, this study examines the nature of CISe NC defects and the implications of these defects on the future of CISe in the PV industry.

Acknowledgments

I would like to thank Dr. Jackson Stolle, whose support and guidance made this thesis possible. I would also like to thank my supervising professor, Dr. Brian Korgel, for his insights and encouragement, and for giving me the space to explore life as a pseudo-graduate student. Many thanks are due to Cherrelle Thomas for her patience, training, and support, and to Dan Houck, Emily Adkins, Xiaotang Lu, Yixuan Yu, and Vikas Reddy, without whom my data would be very sparse. I would also like to acknowledge Douglas Pernik, Dorothy Silbaugh, Adrien Guillaussier, and the Korgel group in general for their insight and willingness to lend a helping hand when I needed it, and Jon Peck, without whom this research group could not function.

Thank you to Dr. D'Arcy Randall, for her support and optimism, which were a bright light when I needed it. Finally, I would be remiss if I did not acknowledge Dr. Matthew West, without whom I might have given up on research altogether three years ago, and my friends and family for their love and support for the last twenty-one years.

Table of Contents

List of Tables

List of Figures

1. Introduction

1.1 Introduction to Photovoltaics

Photovoltaic (PV) devices, also known as solar cells, convert sunlight directly to electricity. The environmental, economic, technical, and political benefits of sunlight as a free and widely available energy resource have long been clear and well-documented.[1-3] As concern grows over environmental impact, depletion of traditional nonrenewable energy sources, and an increase in the energy usage of developing countries, it becomes more important to utilize solar energy. [2] However, the high costs of solar energy technologies relative to conventional energy technologies continue to limit its use; in 2010, solar energy met less than 0.1% of U.S. electricity needs. [1, 4] The U.S. Department of Energy (DOE) estimated that if the price of solar energy decreased 75% between 2010 and 2020 to about $1 per Watt of electricity generated ($1/W), solar energy could become a significant part of the U.S.'s energy future, meeting 14% of U.S. electricity needs by 2030 and 27% by 2050. [1, 3] These estimates depend upon technological advances to address existing challenges, including the tradeoff between cost and efficiency. [1]

1.2 Device Physics

PV devices utilize the electrical properties of semiconductors when exposed to light. The most common model to explain these properties is the band model, in which a solid material is described as consisting of two energy bands, or groups of closely spaced electron states, separated by a band gap. [5] The lower energy band is called the valence band, and the higher energy band is called the conduction band (see Figure 1.1). [6] The band gap, E_g, represents the minimum amount of energy needed to promote an electron from the valence band to the conduction band. When an electron is promoted to the conduction band and becomes a free

electron, a corresponding positively-charged hole is formed in the valence band. [6] Therefore, when light strikes a semiconductor material, all wavelengths of light corresponding to energies $\geq E_g$ will create free electrons, which in turn can create a current and produce electricity.

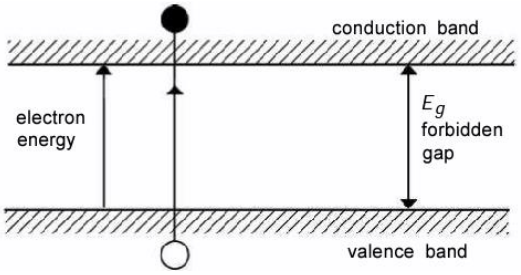

Figure 1.1. Energy level diagram of semiconductor materials. E_g, or forbidden gap, is also referred to as the band gap in this paper, and the conduction and valence bands are also known as E_c and E_v, respectively. [6]

A solar cell consists of two contact layers separated by a light-absorbing semiconductor layer, where one contact layer is optically transparent to allow light through (see Figure 1.2A). Semiconductors are often classified as p-type or n-type; p-type materials contain more holes than electrons, and n-type materials contain more electrons than holes. A piece of a semiconductor can be doped with other materials so that within the same piece, one side is n-type and the other side is p-type. [5] When this happens, a p-n junction is formed where the n-type and p-type sides meet, and creates an electric field that pushes free electrons in the direction of the n-type side, and holes in the direction of the p-type side (see Figure 1.2B). The continuous flow of free electrons ensures a consistent photocurrent and source of electricity. [7] The p-n junction can also be emulated by interfacing a p-type material with an n-type material to form a heterojunction. The semiconductor layer in a solar cell contains either a p-n junction or a heterojunction; the latter is shown in Fig. 1.2A.

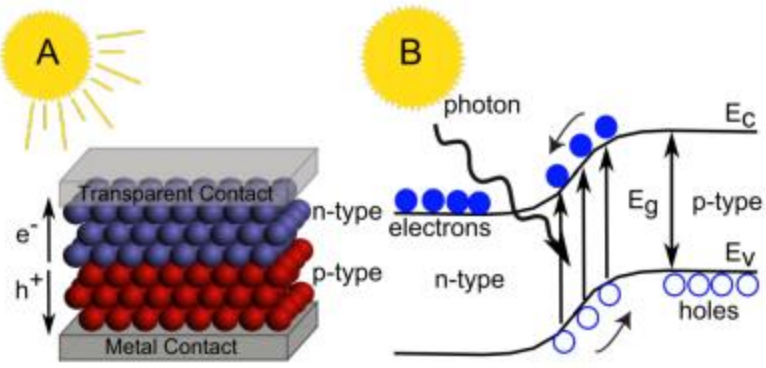

Figure 1.2. (a) A PV device layer consisting of a heterojunction between n-type and p-type nanocrystals, sandwiched between a top transparent contact and a bottom metal contact. **(b)** Energy level diagram of a p-n junction, where the electrons and holes move out of the p-n junction to create a photocurrent. [7]

Although many different kinds of efficiencies are used to evaluate semiconductor materials for photovoltaic applications, the general efficiency of any device typically refers to its power conversion efficiency (PCE, η). PCE measures how much of the solar energy coming in is actually converted to electricity by the device, as shown in Equation 1, where P_{max} is the maximum power output of the device and P_{in} is the power provided by the sun, typically 100 mW/cm^2.

$$\eta = \frac{P_{max}}{P_{in}} \quad (1)$$

Due to spectrum losses, blackbody radiation, and recombination, it is impossible for any device to achieve 100% efficiency. The actual efficiency limit of single-junction solar cells is known as the Shockley-Queisser limit. [3] Spectrum losses and blackbody radiation are out of the scope of this thesis, but efficiency losses occur when electron-hole pairs recombine before current is collected from the electrons. [6] There are three types of recombination – radiative, Auger, and defects – but this thesis focuses on recombination through defects, or trap states, which can occur when impurities within the material or on the surface of the material create

energy levels in the band gap, allowing electrons first to relax to the defect energy level, and then to recombine with the hole at the valence band (see Figure 1.3). [6] In comparison, when radiative recombination occurs, the electron relaxes directly to the valence band, and the difference in energy is given off as a photon, resulting in luminescence. Defects make it easier for recombination to occur before any current is collected from the electron, and result in non-luminescent recombination because the electron does not relax directly to the valence band. [6]

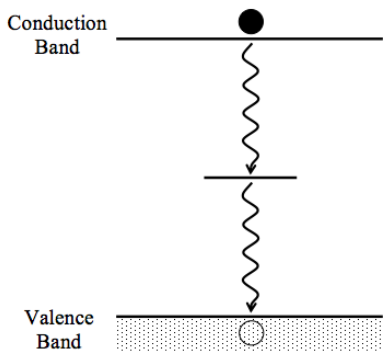

Figure 1.3. A defect, or trap state, creates a new energy level in the band gap that results in recombination efficiency losses.

The more defects there are, the greater the chances of recombination through defects occurring, and therefore the lower the overall efficiency. [6]

1.3 SILICON PHOTOVOLTAICS

Since Bell Labs developed the first modern solar cell in 1954 by using the p-n junction in silicon, silicon has been the dominant technology in PV devices. [8] The current record efficiency is 25.6% for a single-junction crystalline silicon solar cell, and 22.9% for a crystalline silicon module (i.e. a commercial solar panel). [9] In comparison, the Shockley-Queisser limit for silicon is 32.7%, but 29% is considered a more practical limit. [3] As the efficiency of silicon modules has

increased, the cost of production has decreased from around $2/W to just under $1/W in the last few years. [1]

Silicon-based technologies currently comprise about 90% of the PV market, with thin-film technology accounting for the other 10%. [10] Due to the maturity and dominance of silicon, most existing power electronics (to convert the generated DC electricity into AC electricity for consumption or transmission) and balance of systems (the rest of the components and procedures to complete the system, including installation and permitting costs) were designed with silicon technology in mind. [1] In order for other technologies to make significant gains in the PV market, they must be significantly cheaper to produce on a per Watt basis, or reduce balance of systems costs while still achieving commercially viable efficiencies. [1, 3] Therefore, it is important to understand the mechanisms and limitations of promising materials and technologies that have the potential to reduce costs and fuel the growth of solar energy.

1.4 $CuInSe_2$ Nanocrystal Photovoltaics

Thin film and nanocrystal photovoltaics offer one promising alternative to silicon-based technologies because they utilize materials that absorb light better than silicon, and therefore thinner semiconductor layers are needed. As the amount of materials required to build solar cell layers decreases, a thinner substrate, or solar cell base, may also be used. New technologies have begun exploring thinner, cheaper, and flexible plastic substrates instead of the traditional glass substrates. [11, 12] Thin film solar cells have achieved efficiencies that are comparable to silicon, with record efficiencies of over 20% for CIGS and CdTe. [13, 14] However, despite the savings in materials, the processing costs of thin film materials are still too high to pose a significant challenge to silicon's dominance. The main distinction between thin film and nanocrystal

photovoltaics is that thin film solar cells still utilize bulk semiconductor materials, just in smaller quantities, while nanocrystal photovoltaics use semiconductor nanocrystals inks. [7, 15]

One of the key differences between bulk and nanocrystal semiconductors is that when nanocrystals are smaller than approximately 10 nm, they enter the range of quantum confinement, where the energy band gap begins to increase as the nanocrystal size decreases. The continuous conduction and valence energy bands also begin to separate into discrete energy levels (see Figure 1.4). [16] Nanocrystals smaller than 10 nm and quantum confined are also referred to as quantum dots (QDs).

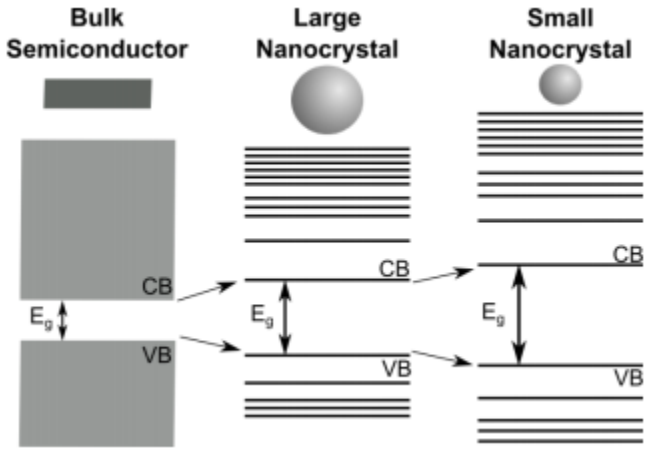

Figure 1.4. An illustration of how the electronic structure of a semiconductor changes due to quantum confinement. The energy levels go from one continued energy band to quantized energy levels that shift with size. [7]

Some of the most well-studied nanocrystals include CdTe,[17-19] $Cu(In,Ga)Se_2$ (CIGS), [20] $Cu_2(Zn,Sn)S_4$ (CZTS), [21] Cu_2S, [22] PbSe, [23] and PbS. [24] This thesis focuses specifically on $CuInSe_2$ (CISe) NCs, which are a subgroup of CIGS NCs. CIGS is widely used and studied for solar cells because it absorbs light very well, is stable in light, and has a tunable band gap (1.04-1.68 eV, depending on the Ga content). [7] This band gap is important because it is within the optimal band gap range for all single junction PV devices of 1.3-1.4 eV. [25] The band gap of bulk CISe is 1.04

eV, but as discussed above, synthesizing CISe QDs can bring the band gap of the CISe QDs closer to 1.3-1.4 eV.[7] Out of all of the nanocrystals that have been studied for PV applications, only CdTe-based devices have a higher efficiency than CIGS-based devices.[13, 14]

However, CISe PV devices made with spray-coated NCs in ambient conditions have exhibited significantly lower efficiencies (3%), due in part to relatively poor electron and hole transport and extraction.[26] While these properties have generally been attributed to bulky ligands, it has been well documented that defects within CISe are to be expected.[27, 28] One of the reasons for these defects is that CISe tolerates a large range of off-stoichiometry without a significant effect on the electronic properties of CISe, creating many opportunities for defects to form.[29, 30]

1.5 CORE/SHELL NANOCRYSTALS

With such small nanocrystals, the surface area to volume ratio is very high, so the surface properties of semiconductor nanocrystals have significant implications on the properties of the NCs as a whole. The surface states of NCs have been known to have poor photostability and quantum efficiency, suggesting that there are trap states, or defects, on the surface resulting in non-radiative recombination.[31] Consequently, these surface defects reduce the fluorescence quantum yield (QY) of the nanocrystals, leading to the use of QY as a measure of the effective passivation of surface defects.[31-33] One strategy to account for these surface defects is to grow a shell of a second semiconductor material around a core of the original NC, thereby passivating the surface defects of the core NCs and increasing the luminescence of the NCs.[32, 34] As a physical barrier, a shell also serves to protect the core from surface chemistry, photo-oxidation, and environmental changes.[35] Core/shell nanocrystals can be classified based on their energy-level alignment, which depends on the interaction between the core and shell materials.[35]

Because the addition of a shell can significantly increase the fluorescence QY of the core nanocrystal, core/shell NCs have primarily been studied for biological labeling, medical imaging, and light-emitting diodes. [35-38]

Although there has been some research on using core/shell nanocrystals for the transparent conducting oxide layer in solar cells, [39] and CdTe/CdSe and CdSe/ZnTe NCs for potential PV device applications, [40] there have been no significant developments in core/shell NCs for PV applications in over a decade. However, more recent studies on core/shell NCs have utilized materials that are also studied for PV applications, including $CuInS_2$ and CdTe. [32, 34, 37] Current synthesis methods for CISe nanocrystals produce weakly luminescent NCs, suggesting that surface defects may be present. [20, 41] Previous research on defects in CISe NCs has not made the distinction between surface and internal defects, [27-30] and what little research there is on CISe-based core/shell NCs has focused on biolabeling and imaging applications. [42, 43]

2. Objectives and Overview

CISe PV devices made with spray-coated nanocrystals in ambient conditions provide many advantages from cost and processing perspectives in comparison to CISe PV devices made with bulk CISe. [7, 15] However, the low efficiencies achieved with spray-coated NCs thus far limit the commercial viability of these devices. [26] Although defects in CISe NCs have been documented before, research has not delineated between surface and internal defects, [27-30] and studies using core/shell NCs have not focused on CISe-based NC, nor on utilizing core/shell NCs for photovoltaics. [42, 43] Creating CISe-based core/shell NCs serves a two-fold purpose: 1) the photoluminescence (PL) of the core/shell NCs can be compared to the PL of the CISe NCs to determine whether the shells passivated the surface defects and therefore increased the efficiency of the CISe NCs; and 2) the internal defects of the CISe NCs can be characterized without compromising the integrity of the NCs. This thesis aims to use CISe-based core/shell NCs to examine the nature of CISe NC defects and the implications these defects may have on the future of CISe in the PV industry.

Chapter 3 provides an overview of the methodology used to synthesize CISe/ZnS core/shell nanocrystals and the techniques and instrumentation used to characterize the core/shell nanocrystal properties. Chapter 4 discusses the data and its implications. Chapter 5 provides overall conclusions and future directions for this research.

3. Experimental Methods

3.1 MATERIALS

The following table displays the list of chemicals used, their purity, and their source.

Table 3.1. Purity and sources of materials used.

Chemical	Purity (%)	Source
Copper (I) chloride (CuCl)	99.99	Aldrich Chemical Co.
Selenium (Se)	99.99	Aldrich Chemical Co.
Zinc stearate (Zn stearate)	Technical grade	Aldrich Chemical Co.
Diphenyphosphine (DPP)	98%	Aldrich Chemical Co.
1-Dodecanethiol (DDT)	≥98	Aldrich Chemical Co.
Trioctylphosphine (TOP)	97%	Aldrich Chemical Co.
Octadecene-1 (ODE)	90%	Aldrich Chemical Co.
Indium (III) chloride ($InCl_3$)	99.99	Strem Chemical
Oleylamine (OLA)	N/A	TCI America or Aldrich Chemical Co.
Toluene	99	Fisher Scientific
Ethanol (EtOH)	Absolute	Fisher Scientific

Prior to use, oleylamine from Aldrich was degassed overnight under vacuum at 110°C. All other chemicals were used as received without further purification or modification. Trioctylphosphine, diphenylphosphine, and degassed oleylamine were stored in an N_2-filled glovebox. Copper (I) chloride, indium (III) chloride, and 1-dodecanethiol were stored in a dessicator.

3.2 $CuInSe_2$ Nanocrystal Synthesis

This procedure was based on a CISe synthesis procedure previously developed by other researchers in this group. [28] In ambient conditions, 2 mmol of CuCl, 2 mmol of $InCl_3$, and 20 mL of OLA were added into a 3 neck flask with a stir bar. The DPP:Se solution was made separately by mixing 2 mmol of Se with 2 mL of DPP, and diluted with 2 mL of OLA. The flask was sealed with septa and wire, and attached to a Schlenk line equipped with a stir plate and a heating mantle. The reaction mixture was stirred and heated to 110°C under vacuum for at least an hour, until the mixture was a light yellow color. The flask was then backfilled with nitrogen and heated to 150°C. When the solution temperature was stabilized at 150°C, the DPP:Se solution was injected, forming a dark brown or black solution, and the reaction continued for one hour at 150°C (see Figure 3.1).

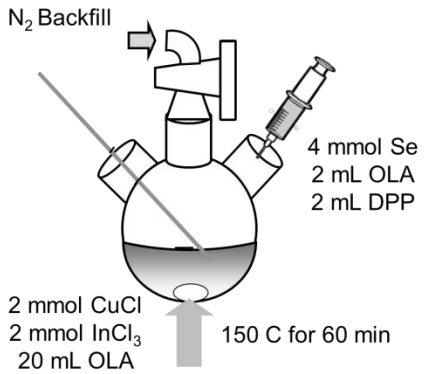

Figure 3.1. Diagram of the DPP injection, $CuInSe_2$ nanocrystal synthesis method.

After an hour, the solution was separated into two centrifuge tubes, and the nanocrystals were precipitated out of solution by adding 20 mL of ethanol to each tube and centrifuged at 6000 RPM for 5 minutes. The supernatant was discarded and the precipitate was redispersed by adding 10 mL of toluene to each tube, mixing for less than a minute on a vortex mixer, and sonicating in a water bath for 5 minutes. Poorly-capped NCs were then precipitated out of

solution by centrifuging at 6000 RPM for 5 minutes. The supernatant was transferred to new centrifuge tubes, and ethanol was added slowly until the first NCs began to precipitate out of solution (usually 10-15 mL). The mixture was then centrifuged again at 6000 RPM for 5 minutes, and the supernatant was discarded. The precipitate (the CISe NCs) was redispersed in toluene and sonicated for 15 minutes in a water bath. The solution was dried on a rotovap to measure the yield, redispersed again in enough toluene to make a concentration of 50 mg CISe/mL solution, and stored in an N_2-filled glovebox.

3.3 ZnS Overcoating

This procedure was based on an overcoating procedure developed to put ZnS and CdS shells on a $CuInS_2$ core.[32] To prepare the CISe NCs, 1 mL of the 50 mg CISe/mL solution was removed from the glovebox and mixed with 10 mL of ethanol. The mixture was centrifuged at 6000 RPM for 5 minutes to precipitate the NCs out of solution. The supernatant was discarded and the precipitate was redispersed in 1 mL of DDT and diluted with 4 mL of ODE. This solution was then transferred to a 3 neck flask with a stir bar, sealed with septa and wire, and transferred to a Schlenk line equipped with a stir plate and heating mantle. The ZnS precursor solution was prepared separately by mixing 1.13 mmol of Zn stearate with 1.13 mL of a 1 M S in TOP solution and diluting with 11.3 mL of ODE. The reaction mixture was degassed three times, then backfilled with nitrogen and heated to 210°C. When the mixture temperature was stabilized at 210°C, the ZnS precursor solution was slowly injected into the flask at a rate of 12 mL/hr (see Figure 3.2).

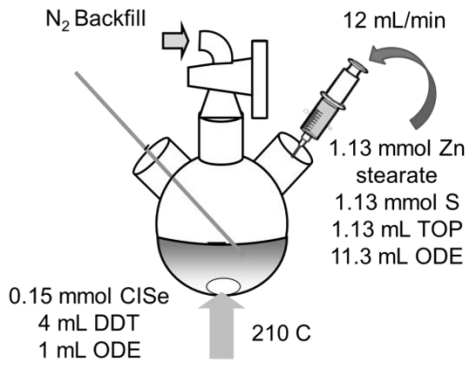

Figure 3.2. Diagram of the slow injection ZnS overcoating procedure.

After the ZnS precursor solution was completely injected, the reaction solution was separated into two centrifuge tubes and 20 mL of ethanol was added to each tube before centrifuging at 6000 RPM for 5 minutes. The supernatant was discarded and the precipitate was redispersed in 10 mL of toluene, mixed on a vortex mixer for less than 1 minute, and sonicated in a water bath for 5 minutes. Poorly-capped NCs were then precipitated out of solution by centrifuging at 6000 RPM for 5 minutes. The supernatant was transferred to another centrifuge tube, and ethanol was added slowly until the first NCs began to precipitate out of solution (usually 15-20 mL). The mixture was then centrifuged at 6000 RPM for 5 minutes. The redispersion of the precipitate in toluene, crashing out of poorly-capped NCs, and washing in ethanol were all repeated two more times before the nanocrystals were again redispersed in toluene, sonicated for 15 minutes in a water bath, and stored in an N_2-filled glovebox.

3.4 Other Samples

To redisperse CISe in DDT in a manner similar to the overcoating procedure, 0.5 mL of the 50 mg CISe/mL solution was removed from the glovebox and mixed with 10 mL of ethanol. The mixture was centrifuged at 6000 RPM for 5 minutes to precipitate the NCs out of solution.

The supernatant was discarded and the precipitate was redispersed in 0.5 mL of DDT and diluted with 2 mL of ODE. Only 10 mL of ethanol was added instead of 20 mL, but otherwise the washing method for the overcoating procedure was repeated.

To simulate a situation in which only the zinc reacted to form a zinc-based complex on the surface of the nanocrystals, 0.5 mL of the 50 mg CISe/mL solution was removed from the glovebox and mixed with 10 mL of ethanol. The mixture was centrifuged at 6000 RPM for 5 minutes to precipitate the NCs out of solution. The supernatant was discarded and the precipitate was redispersed in 0.5 mL of DDT and diluted with 2 mL of ODE. The Zn precursor consisted of 0.56 mmol of Zn stearate mixed with 5.6 mL of ODE, and the Zn precursor was added to the solution before sonicating the solution for around 30 minutes. Only 10 mL of ethanol was added instead of 20 mL, but otherwise the washing method for the overcoating procedure was repeated.

3.5 Samples and Procedural Modifications

Two batches of $CuInSe_2$ nanocrystals were made using the same procedure described above with two specific modifications. The scale of the first batch, 'CISe (23 Jan)', was double the procedure, so the target was 4 mmol of CISe instead of 2 mmol. The second batch, 'CISe (16 Feb)', was made using Aldrich oleylamine instead of the TCI oleylamine used for the first batch, due to material and time constraints. 'CISe/ZnS (4 Feb)', 'CISe/ZnS (6 Feb)', and 'CISe/ZnS (11 Mar)' were all made using CISe (23 Jan) as the core, and 'CISe/ZnS (23 Feb)' was made using CISe (16 Feb) as the core. 'CISe/DDT (8 Apr)' and 'CISe/DDT/Zn (3 Apr)' were also made using CISe (23 Jan) (see Figure 3.3).

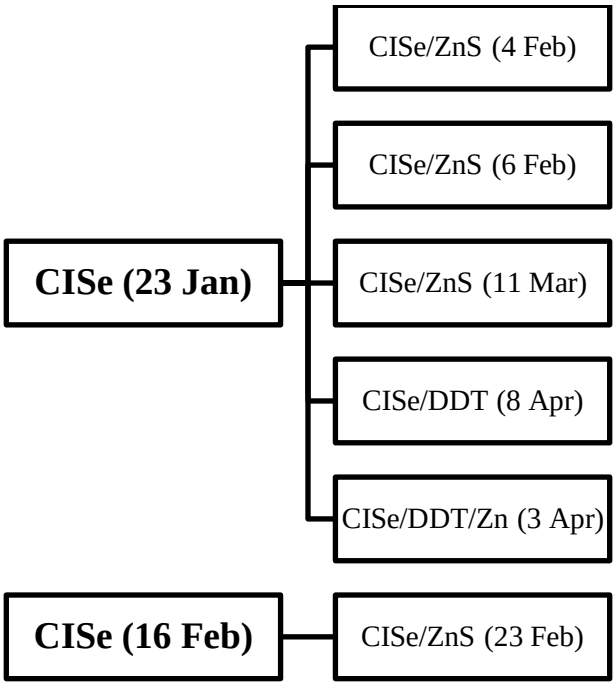

Figure 3.3. Diagram of the samples associated with each core CISe nanocrystal sample.

CISe/ZnS (6 Feb) and CISe/ZnS (23 Feb) were both coated using the same procedure described above with no deliberate modifications, but CISe/ZnS (4 Feb) was coated with half of the quantity of ZnS precursor described in the procedure, so a thinner shell is expected. Due to limited quantities, not every sample was tested using every characterization technique, but the trends within each set of samples were expected to be consistent within other sets of samples.

3.6 Characterization Techniques

UV-Vis-NIR absorbance data were taken using a Cary 500 spectrophotometer. Photoluminescence data were taken using a Fluorolog3 fluorimeter with a single grating Czerny-Turner IR emission spectrometer. XRD was collected on a Rigaku R-Axis Spider diffractometer equipped with a Bruker Sol-X Si(Li) solid state detector and 1.54 Å radiation (Cu Kα). Data were collected at 0.01 increments of 2θ at a scan rate of 6°/min. Transmission electron

microscope (TEM) images were collected with a FEI Tecnai G2 Spirit BioTwin microscope operating at 80 kV. High resolution transmission electron microscope (TEM) images and energy-dispersive X-ray spectrometry (EDS) data were collected with an Oxford INCA EDS dectector on a JEOL 2010F microscope. X-ray photoelectron spectrometry (XPS) data were taken with a Kratos Axis Ultra DLD x-ray photoelectron spectrometer.

4. Results and Discussion

4.1 CISe/ZnS Nanocrystal Size and Quantum Confinement

TEM images were taken to visually determine the physical characteristics of the nanocrystals, including the size. The overcoating procedure led to a significant increase in the size of the NCs relative to the CISe NC baseline for one set of samples, while another set of samples had an insignificant increase in size. The amount of ZnS precursor was calculated to produce a shell with a thickness of approximately 1 nm, so the expected total difference in size is 2 nm. The average differences in the size of the CISe particles before and after the overcoating procedure were 1.20±0.36 nm [CISe (23 Jan)] (see Figure 4.1) and 0.09±0.31 nm for [CISe (16 Feb)] (see Figure 4.2).

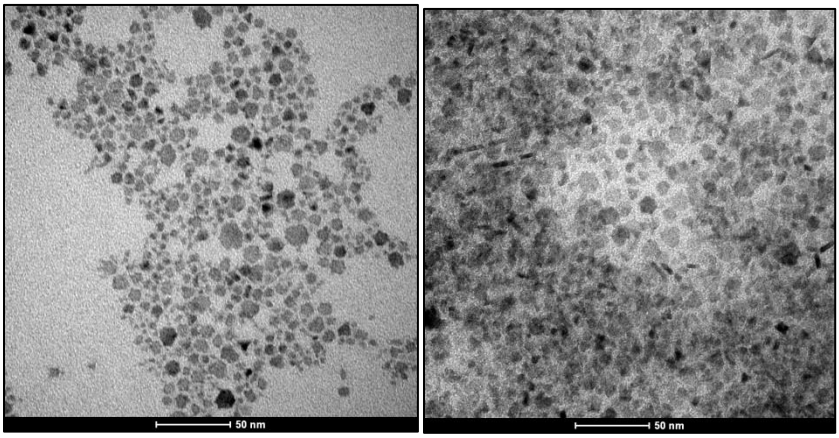

Figure 4.1. TEM images with a 50 nm scale. **(a)** CISe (23 Jan), with an average nanocrystal size of 4.73±1.07 nm and some aggregation of particles. **(b)** CISe/ZnS (6 Feb), with an average nanocrystal size of 6.93±0.92 nm. Aggregation of particles is present, and the image looks "dirty" due to leftover organic residue that was not completely removed by the washing procedure.

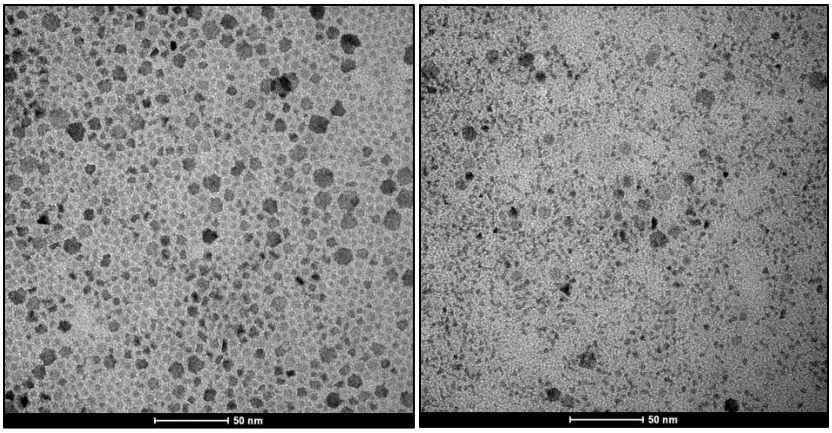

Figure 4.2. TEM images with a 50 nm scale. **(a)** CISe (16Feb), with an average nanocrystal size of 3.89±0.85 nm, and some aggregation of particles. **(b)** CISe/ZnS (23Feb), with an average nanocrystal size of 3.97±0.99 nm.

There was a definite increase in the size of the nanocrystals before and after the overcoating procedure on the CISe (23Jan) samples, but not on the CISe (16 Feb) samples. This result suggests that the ZnS precursor may have formed shells around the CISe NCs, but not uniformly. It is possible that the original CISe NCs were etched when redispersed in DDT, which would result in smaller NCs, and when the shell formed, it made up for the difference in size before and after the original NCs were etched. Another explanation for the discrepancy between the expected and actual differences in size is excess ZnS precursor that did not react to form part of the shell during the overcoating reaction, or was removed from the surface of the shell during the washing process. Although high-resolution TEM (HR TEM) was utilized to try to provide clearer images than those provided in Figures 4.1 and 4.2, there were issues with drift in the HR TEM that resulted in pictures that were less clear than those obtained with the low-resolution TEM.

To verify that the CISe nanocrystals were not significantly affected by the overcoating procedure, UV-Vis absorption spectra of the samples were taken (see Figures 4.3 and 4.4). Because the band gap of bulk ZnS is 3.68 eV, which corresponds to an absorbance spectra

starting around 337 nm, ZnS cannot be detected when CISe is also present, because bulk CISe has a band gap of 1.04 eV, which corresponds to an absorbance spectra starting at 1190 nm. Therefore UV-Vis was not a good technique to determine the presence of ZnS, but if the CISe NCs were compromised by the overcoating procedure, it would be expected that the absorbance spectra of the CISe NCs before and after the overcoating procedure would be different.

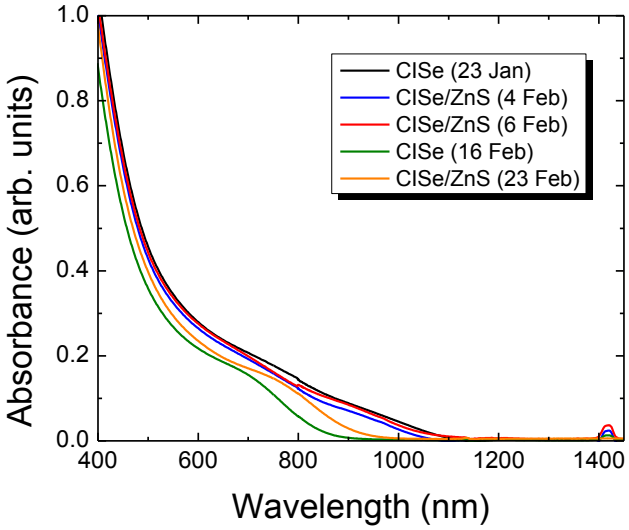

Figure 4.3. UV-Vis absorption spectra of CISe (23 Jan), CISe/ZnS (4 Feb), CISe/ZnS (6 Feb), CISe (16 Feb), and CISe/ZnS (23 Feb).

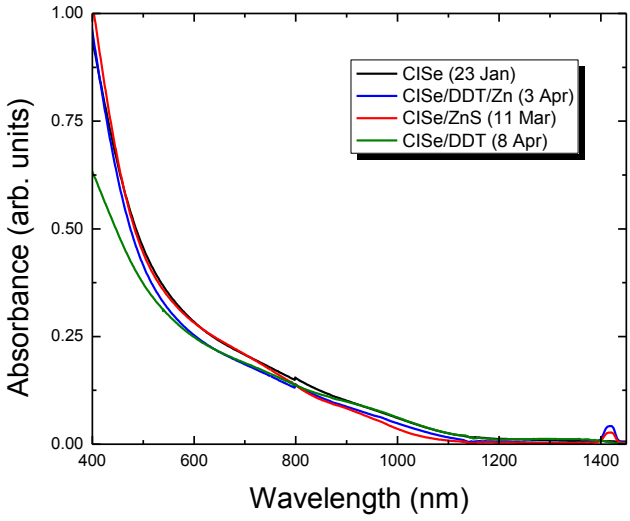

Figure 4.4. UV-Vis absorption spectra of CISe (23 Jan), CISe/ZnS (11 Mar), CISe/DDT/Zn (3 Apr), and CISe/DDT (8 Apr).

For all of the CISe/ZnS samples with a CISe (23 Jan) core, there were no significant differences between the UV-Vis spectra for the CISe/ZnS samples and the CISe (23 Jan) sample. The UV-Vis spectra also suggests that the band gap for all of these samples is around 1080 nm, based on where the absorption peak begins. In Fig. 4.3, the spectra for the CISe (16 Feb) sample and its corresponding CISe/ZnS (23 Feb) differ noticeably from the other samples, mainly with regards to the shoulder in the peak, and where the absorption peak begins. These differences are both attributable to changes in the NC size.

Due to quantum confinement, when the nanocrystal size decreases, the band gap increases, so the wavelength where the absorption peak begins would be expected to decrease, because band gap energy and wavelength are inversely proportional to each other. As seen in Figures 4.1 and 4.2, the CISe (16 Feb) sample was smaller than the CISe (23 Jan) sample, so the UV-Vis spectra confirms that the NCs were small enough for quantum confinement to occur. The other benefit that quantum confinement, in conjunction with UV-Vis, offers is that it makes it clearer that the CISe/ZnS (23 Feb) NCs are larger than the CISe (16 Feb), which was not clear from the TEM images. The CISe (16 Feb) spectra blue-shifted – which means the spectra shifted to smaller wavelengths and thus a higher energy band gap – more than the CISe/ZnS (23 Feb) spectra, providing clearer evidence that the overcoating procedure increased the size of the NCs.

4.2 CISe/ZnS Nanocrystal Shell Growth

In order to verify that the CISe nanocrystals were not compromised by the overcoating procedure, and that the increase in the size of the NCs was due to the addition of ZnS, XRD patterns were taken of the samples. For all of the samples, the peaks in the XRD pattern corresponded to the peaks expected for chalcopyrite CISe (a specific crystal structure for CISe),

suggesting that the CISe synthesis did produce CISe NCs, and the overcoating did not affect the CISe core. However, there was no difference between the XRD patterns of the CISe samples and the CISe/ZnS samples, and no peaks that corresponded to the pattern for ZnS (see Figure 4.5). While the lack of ZnS peaks could certainly mean that the increase in size was not due to the addition of ZnS, it may also just be due to the thickness of the (presumed) ZnS shell. In order for an XRD peak to be visible, there must be at least two atomic layers of the material available. The average thickness of a ZnS monolayer is 0.31 nm, and the average thicknesses of the shells formed were 0.60 nm and 0.045 nm, so even if a ZnS shell was present, the ZnS would most likely not be detected by XRD.

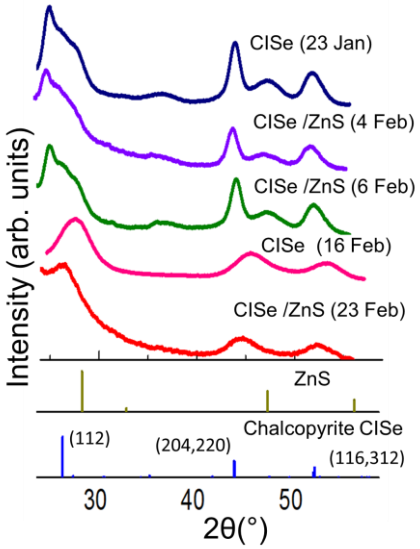

Figure 4.5. XRD patterns of CISe (23 Jan), CISe/ZnS (4 Feb), CISe/ZnS (6 Feb), CISe (16 Feb), and CISe/ZnS (23 Feb), with ZnS and chalcopyrite CISe reference patterns for comparison.

XPS, on the other hand, showed a clear difference between the samples with and without shells (see Figure 4.6). Because XPS is an elemental analysis, the peaks do not correspond to specific compounds, only specific elements. In the samples without a shell, there are definitive peaks for copper and indium, and a peak that may be sulfur or selenium, because the sulfur and

selenium patterns overlap very closely in XPS. However, there was no source of sulfur in the CISe synthesis procedure, so the peak most likely corresponds to selenium, as expected.

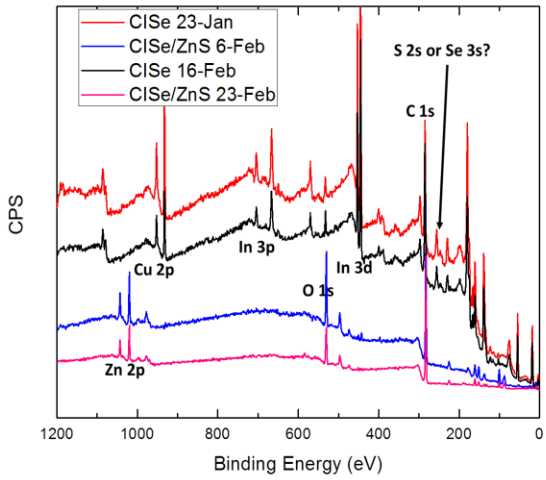

Figure 4.6. XPS spectra of CISe (23 Jan), CISe/ZnS (6 Feb), CISe (16 Feb), and CISe/ZnS (23 Feb). The peaks for CISe (23 Jan) and CISe (16 Feb) at around 250 eV marked "S 2s or Se 3s?" is presumed to be Se 3s.

In the samples with a shell, the copper, indium, and selenium peaks all disappear, and peaks corresponding to zinc, oxygen, and carbon appear. The presence of the carbon peak suggests that the washing procedure for the CISe/ZnS nanocrystals was not sufficient to remove all of the organic compounds. The presence of the oxygen peak indicates that the samples may have oxidized when they were left in ambient conditions for a few days while waiting for testing, but this explanation seems insufficient given the lack of a clear sulfur peak, which still should have been present even if the ZnS oxidized. While the disappearance of the copper, indium, and selenium peaks provide clear evidence that the CISe NCs were completely covered by another Zn-based layer, it is still surprising that no clear copper, indium, or selenium peaks appear at all, given the relatively small thickness of the outer shell.

To further investigate these surprising discrepancies, a high-res TEM (HR TEM) was used to perform an EDS analysis of the samples. Like the XPS, EDS is an elemental analysis, and peaks in EDS spectra correspond to specific elements. EDS detected carbon, nickel, and trace amounts of oxygen, but the TEM grids used consisted of a carbon film on a nickel grid, so carbon and nickel are expected. Unwashed organics and trace amounts of oxygen that were introduced into the EDS or oxidized the grids would also account for the presence of carbon and oxygen. Therefore the final EDS results were corrected for the presence of carbon, nickel, and oxygen, and only show the relative amounts of copper, indium, selenium, zinc, and sulfur detected (see Table 4.1).

Table 4.1. HR TEM EDS results.

Element	**CISe (23 Jan)**	**CISe/ZnS (6 Feb)**	**CISe (16 Feb)**	**CISe/ZnS (23 Feb)**
Copper (atomic %)	34.45	11.88	32.55	17.93
Indium (atomic %)	28.94	9.95	28.30	15.53
Selenium (atomic %)	36.61	14.69	39.15	22.87
Zinc (atomic %)	-	34.70	-	25.72
Sulfur (atomic %)	-	28.79	-	17.96

Based on the chemical formula for $CuInSe_2$ and ZnS, a 1:1:2 ratio of Cu, In, and Se and a 1:1 ratio of Zn and S were expected, but these ratios were not verified by the EDS data. Before correction, carbon and indium comprised 50-90% of the detected elements, so the detected amounts of copper, indium, selenium, zinc, and sulfur were much smaller than the corrected amounts shown in Table 4.1. At small concentrations, performing quantitative EDS analysis is challenging, and any errors in the automatic peak identification software used for the analysis, or in the conditions under which the analysis was performed, could have a significant impact on the

final quantitative EDS results.[44] Therefore, the main purpose of EDS in this thesis was to verify the presence of copper, indium, selenium, zinc, and sulfur in relatively appropriate proportions, but not necessarily the exact chemical formula.

EDS confirmed the presence of copper, indium, and selenium in all of the samples, although selenium was not detected in significantly larger quantities than copper. Similarly, in the CISe/ZnS samples, although both zinc and sulfur were detected, more zinc was detected than sulfur in both samples. It should also be noted that although copper, indium, and selenium were already known to be in a nanocrystal structure, and zinc was only introduced to the zinc sulfide precursor solution, another possible source of sulfur in the samples was DDT, which was used to redisperse CISe NCs before adding the ZnS shell to help the formation of a ZnS shell on the CISe NC surface.

Because the results from XPS and HR TEM EDS were inconclusive, Raman spectroscopy was also used to detect any signs of a ZnS shell and to confirm that the CISe NC cores were unaffected by the overcoating procedure. Raman is a more sensitive test than the other two, so if ZnS was formed, it should be detected by Raman (see Figure 4.7).

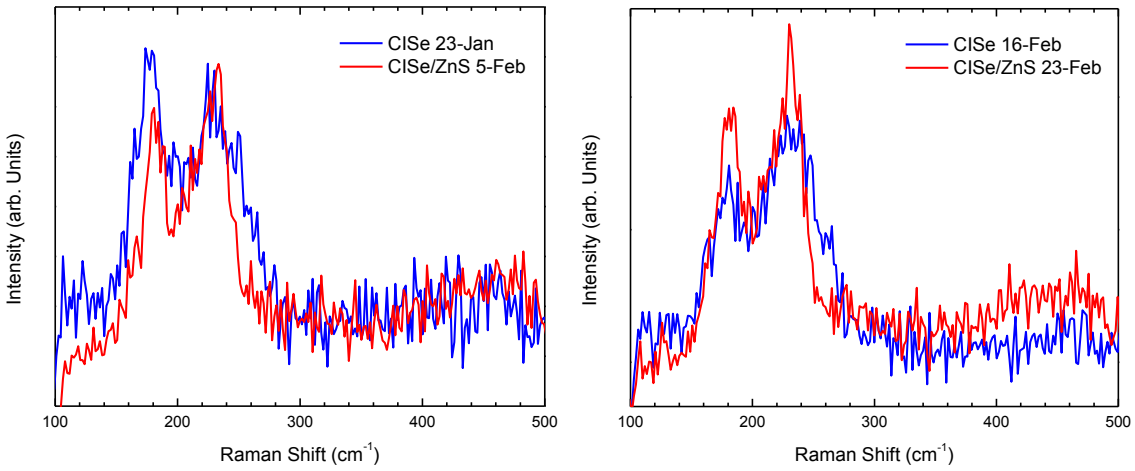

Figure 4.7. Raman spectroscopy data for **(a)** CISe (23 Jan) and CISe/ZnS (6 Feb) and **(b)** CISe (16 Feb) and CISe/ZnS (23 Feb). Only CISe peaks are visible in both spectra.

If there were any ZnS in the CISe/ZnS samples, a clear peak at around 355 cm^{-1} would be expected. Although the Raman spectra are noisy, there is no clear peak at around 355 cm^{-1}, suggesting that whatever formed on the surface of the CISe NCs was not ZnS. Although there are some minor changes in the Raman spectra for samples before and after the overcoating, they are not significant enough to suggest that the CISe NCs were affected by the overcoated procedure; the test is sensitive enough that some variability, even for the same sample, is expected.

When the results from TEM, UV-Vis, XPS, HR TEM EDS, and Raman are all considered together, they suggest that a Zn-based shell, between 0.045 and 0.6 nm thick, was formed around core CISe NCs, and that the composition of the CISe NCs was not significantly compromised by the overcoating procedure. The Zn-based shell was most likely not ZnS, and the sulfur detected by the HR TEM EDS can be attributed to the presence of DDT, a sulfur-based compound used to redisperse the CISe NCs before the overcoating procedure.

4.3 Luminescent CISe-Based Core/Shell Nanocrystals

Although the exact composition of the presumed shell is difficult to verify, the presence of a Zn-based layer nevertheless suggests that there may be a shell that passivated the surface defects of the core CISe nanocrystal. The presence of surface defects can be related to the photoluminescence of the NCs – the fewer surface defects, the more luminescent the NCs, because the passivated surface defects allow for more efficient electron-hole recombination, as discussed earlier.

Next, CISe/DDT and CISe/DDT/Zn samples were made to test whether the overcoating procedure had any significant impact on the passivation of surface defects, or if the procedure was equivalent to simply mixing CISe with DDT and a Zn precursor in ambient conditions. The photoluminescence (PL) of the prospective CISe, CISe/ZnS, and CISe/DDT/Zn samples was measured; the CISe/DDT sample was not measured because the CISe/DDT/Zn sample was the most comparable to CISe/ZnS (see Figure 4.8).

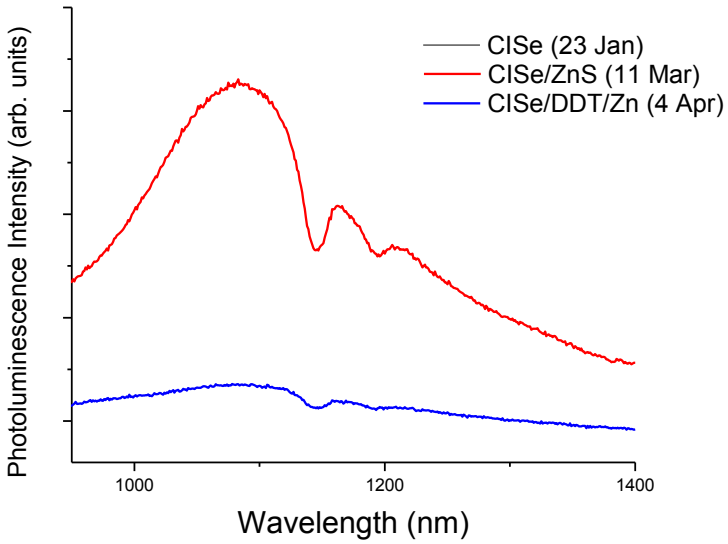

Figure 4.8. Emission spectra of CISe (23 Jan), CISe/ZnS (11 Mar), and CISe/DDT/Zn (4 Apr), with an excitation wavelength of 470 nm and integration time of 0.5 sec. The photoluminescent peak occurs at 1080 nm.

The concentrations of all of the samples were approximated based on the UV-Vis spectra (see Figures 4.3 and 4.4); as a general rule, the samples were diluted until the absorbance was 1.0±0.1 so that the luminescence of the samples could be compared equally. CISe (23 Jan) had no visible luminescence; while there was a broad peak at around 1100 nm for CISe/DDT/Zns. However, the most luminescent sample was definitely CISe/ZnS, which had a clear peak at around 1080 nm, which corresponds with the band gap energy given by UV-Vis (see Figures 4.3 and 4.4). The secondary PL peaks were due to a detector error, and were not actually a part of the

true PL spectra for the samples. Similarly, the same trend occurred for the CISe (16 Feb) and CISe/ZnS (23 Feb) set, where CISe (16 Feb) did not luminesce and CISe/ZnS (23 Feb) luminesced at around 960 nm, which corresponds to the UV-Vis data (see Figure 4.9).

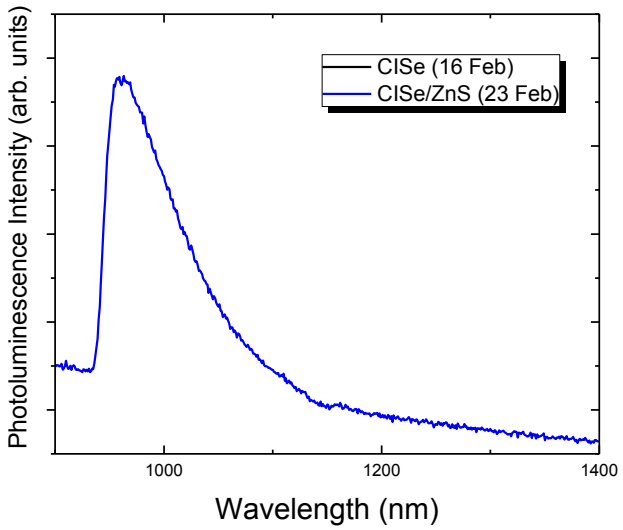

Figure 4.9. Emission spectra of CISe (16 Feb) and CISe/ZnS (23 Feb), with an excitation wavelength of 470 nm and integration time of 0.5 sec. The photoluminescent peak is at 960 nm.

The strong luminescence of the CISe/ZnS samples, especially relative to the CISe/DDT/Zn sample, indicates that the overcoating procedure did have a significant impact on the passivation of surface defects, even if it did not produce the ZnS shell as intended.

4.4 PHOTOVOLTAIC DEVICES

One of the key reasons for investigating the defects of CISe nanocrystals is that they lower the efficiency of CISe-based devices. By passivating the surface defects, the efficiency of CISe-based devices would theoretically increase, but conversely, the ZnS shell used to passivate the surface defects might inhibit the performance of the CISe NCs. Although device performance was not a focus of this thesis, two devices were made using CISe (16 Feb) and CISe/ZnS (23 Feb)

to provide a preliminary data point for future investigations, and the device performance and efficiency were evaluated (see Figure 4.10).

The CISe device had an efficiency of 0.037% and the expected diode behavior under both dark and light conditions, although it was significantly lower than the CISe device efficiencies of 2-3% previously achieved by other researchers in the group (see Figure 4.10A). [20, 28] Unfortunately, visible cracks in the nanocrystal film on the CISe/ZnS device were noticed after drying, and ultimately allowed the top and bottom contacts to touch, creating a shorted device, which was reflected in the current-voltage plot for the device (see Figure 4.10B).

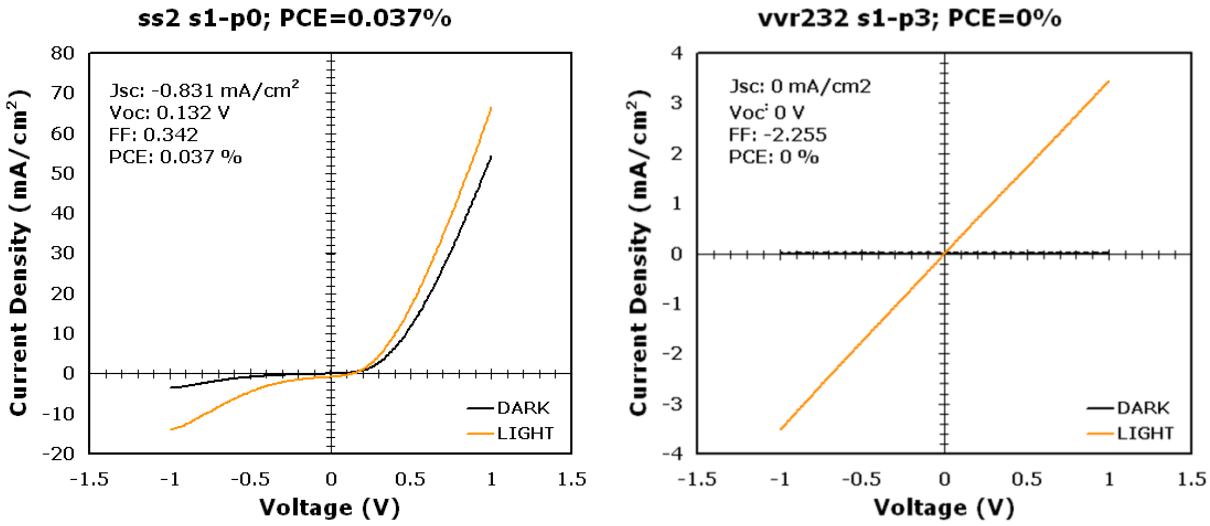

Figure 4.10. Current-voltage plots showing the dark and light photovoltaic responses of devices made with **(a)** CISe (16 Feb) and **(b)** CISe/ZnS (23 Feb).

The shorted CISe/ZnS device meant that no new information could be obtained about the relative performance of a device with the addition of the ZnS shell, and due to a lack of resources, a second set of devices could not be created. Nonetheless it should be remembered that the focus of this project was not on the building, testing, or performance of devices, but rather understanding the properties of the individual CISe NCs.

5. Conclusions and Future Directions

5.1 Conclusions

Although the benefits of solar energy have long been clear, the technology needed to make solar energy a significant portion of the energy production in the United States is still being developed, with most of the focus on advances in thin film and nanocrystal technologies. One class of next generation PV materials being studied is $CuInSe_2$ (CISe), which has many inherent properties that make it a promising candidate for PV applications, but one of its limitations is the presence of defects in CISe NCs, which lower the efficiency of CISe-based devices. Improving the understanding of defects in CISe NCs could help increase the efficiency of CISe, and decrease costs, ultimately leading to broader commercialization of CISe NCs for PV applications.

Although the data suggest that some sort of Zn-based shell was successfully formed around a core CISe nanocrystal without significantly impacting the core NC, the Zn-based shell was most likely not the intended ZnS. However, the Zn-based shell was more substantial than free Zn complexing on the surface of CISe, as evidenced by the luminescence of CISe NCs with free Zn and CISe NCs with a Zn-based shell. The increased luminescence of the CISe/ZnS samples provides evidence that the Zn-based shell successfully passivated many, if not all, of the surface defects on CISe NCs.

5.2 Future Directions

To move forward with this project, it is important to find new ways to characterize and identify the chemical structure of the shell that has formed around the core NC, since it does not seem to be the intended ZnS. Another option is to try different materials, such as CdS, for the

shell, but it is possible that the issue is the procedure, not the materials themselves, so the overcoating procedure should also be revisited and refined.

Although this research demonstrated that the surface defects can be successfully passivated with a shell, more work needs to be done to characterize internal defects. One method to do this would be a lifetime measurement on the luminescent CISe/ZnS NCs relative to the non-luminescent CISe NCs. Although this equipment was not immediately available at the University of Texas at Austin because the luminescence occurred in the IR region, there are resources to test this at Argonne National Laboratory, and there are most likely other options nearby as well.

Finally, the ultimate goal of this research was to produce more efficient, commercially viable CISe-based PV devices. Further testing is needed to understand how the size and composition of a shell will affect the performances of CISe-based PV devices, and to refine the methodology to better control for the size and composition of a shell.

References

1. U.S. Department of Energy. *SunShot Vision Study*, 2012.

2. Dincer, I. Renewable energy and sustainable development: a crucial review. *Renewable and Sustainable Energy Reviews* **2000,** *4,* 157-175.

3. Chu, S.; Majumdar, A. Opportunities and challenges for a sustainable energy future. *Nature* **2012,** *488,* 294-303.

4. Timilsinaa, G. R.; Kurdgelashvili, L.; Narbel, P. A. Solar energy: Markets, economics and policies. *Renewable and Sustainable Energy Reviews* **2012,** *16,* 449-465.

5. Callister, W. D.; Rethwisch, D. G. *Materials Science and Engineering: An Introduction,* 8th ed.; John Wiley & Sons, Inc., 2010.

6. Wenham, S. R.; Green, M. A.; Watt, M. E.; Corkish, R. P.; Sproul, A. *Applied Photovoltaics,* 3rd ed.; Earthscan: New York, NY, 2012.

7. Stolle, C. J.; Harvey, T. B.; Korgel, B. A. Nanocrystal photovoltaics: a review of recent progress. *Curr. Opin. Chem. Eng.* **2013,** *2,* 160-167.

8. Chapin, D. M.; Fuller, C. S.; Pearson, G. L. A New Silicon p-n Junction Photocell for Converting Solar Radiation into Electrical Power. *J. Appl. Phys.* **1954,** *25* (676), 676-677.

9. Green, M. A.; Emery, K.; Hishikawa, Y.; Warta, W.; Dunlop, E. D. Solar cell efficiency tables (version 45). *Prog. Photovol: Res. Appl.* **2014,** *23,* 1-9.

10. Fraunhofer Institute for Solar Energy Systems. *Photovoltaics Report;* Fraunhofer Institute for Solar Energy Systems: Freiburg, 2014.

11. Chirila, A. e. a. Highly efficient Cu(In,Ga)Se2 solar cells grown on flexible polymer films. *Nature Materials* **2011,** *10,* 857-861.

12. Kessler, F.; Herrmann, D.; Powalla, M. Approaches to flexible CIGS thin film solar cells. *Thin Solid Films* **2005,** *480-481,* 491-498.

13. Jackson, P.; Hariskos, D.; Lotter, E.; Paetel, S.; Wuerz, R.; Menner, R.; Wischmann, W.; Powalla, M. New world record efficiency for Cu(In,Ga)Se2 thin-film solar cells beyond 20%. *Prog. Photovolt: Res. Appl.* **2011,** *19* (7), 894-897.

14. First Solar, I. First Solar Builds the Highest Efficiency Thin Film PV Cell on Record, 2014. First Solar. http://investor.firstsolar.com/releasedetail.cfm?ReleaseID=864426 (accessed

April 2015).

15. Kramer, I. J.; Sargent, E. H. Colloidal quantum dot photovoltaics: a path forward. *ACS Nano* **2011,** *5* (11), 8506-8514.

16. Hollingsworth, J. A.; Klimov, V. I. "Soft" Chemical Synthesis and Manipulation of Semiconductor Nanocrystals. In *Semiconductor and Metal Nanocrystals: Synthesis and Electronic and Optical Properties;* Klimov, V. I., Ed.; Marcel Dekker: New York, 2004.

17. Jasieniak, J.; MacDonald, B. I.; Watkins, S. E.; Mulvaney, P. Solution-processed Sintered Nanocrystal Solar Cells via Layer-by-Layer Assembly. *Nano Lett.* **2011,** *11* (7), 2856-2864.

18. Olson, J. D.; Rodriguez, Y. W.; Yang, L. D.; Alers, G. B.; Carter, S. A. CdTe Schottky diodes from colloidal nanocrystals. *Appl. Phys. Lett.* **2010,** *96* (24), 242103.

19. Gur, I.; Fromer, N. A.; Geier, M. L.; Alivisatos, A. P. Air-Stable All-Inorganic Nanocrystal Solar Cells Processed from Solution. *Science* **2005,** *310* (5747), 462-465.

20. Panthani, M. G.; Akhavan, V.; Goodfellow, B.; Schmidtke, J. P.; Dunn, L.; Dodabalapur, A.; Barbara, P. F.; Korgel, B. A. Synthesis of CuInS2, CuInSe2, and Cu(InxGa1-x)Se2 (CIGS) nanocrystal "inks" for printable photovoltaics. *J. Am. Chem. Soc.* **2008,** *130* (49), 16770-16777.

21. Steinhagen, C.; Panthani, M. G.; Akhavan, V.; Goodfellow, B.; Koo, B.; Korgel, B. A. Synthesis of Cu2ZnSnS4 Nanocrystals for Use in Low-Cost Photovoltaics. *J. Am. Chem. Soc.* **2009,** *131* (35), 12554-12555.

22. Wu, Y.; Wadia, C.; Ma, W.; Sadtler, B.;. Alivisatos, A. P. Synthesis and Photovoltaic Application of Copper (I) Sulfide Nanocrystals. *Nano Let.* **2008,** *8* (8), 2551-2555.

23. Choi, J. J. e. a. PbSe Nanocrystal Excitonic Solar Cells. *Nano Lett.* **2009,** *9* (11), 3749-3755.

24. Chuang, C. M.; Brown, P. R.; Bulovic, V.; Bawendi, M. G. Improved performance and stability in quantum dot solar cells through band alignment engineering. *Nature Materials* **2014,** *13,* 796-801.

25. Henry, C. H. Limiting efficiencies of ideal single and multiple energy gap terrestrial solar cells. *J. Appl. Phys.* **1980,** *51,* 4494.

26. Akhavan, V. A.; Panthani, M. G.; Goodfellow, B. W.; Reid, D. K.; Korgel, B. A. Thickness-limited performance of CuInSe2 nanocrystal photovoltaic devices. *Opt. Express* **2010,** *18,* A411-A420.

27. Akhavan, V. A.; Goodfellow, B. W.; Panthani, M. G.; Steinhagen, C.; Harvey, T. B.; Stolle, C. J.; Korgel, B. A. Colloidal CIGS and CZTS nanocrystals: A precursor route to printed photovoltaics. *J. Solid State Chem.* **2012,** *189*, 2-12.

28. Akhavan, V. A.; Goodfellow, B. W.; Panthani, M. G.; Reid, D. K.; Hellebusch, D. J.; Adachi, T.; Korgel, B. A. Spray-deposited CuInSe2 nanocrystal photovoltaics. *Energy Environ. Sci.* **2010,** *3* (10), 1600-1606.

29. Wei, S. H.; Zhang, S. B. Defect properties of CuInSe2 and CuGaSe2. *J. Phys. Chem. Solids* **2005,** *66* (11), 1994-1999.

30. Von Bardeleben, H. J. The chemistry of structural defects in CuInSe2. *Solar Cells* **1986,** *16*, 381-390.

31. Yang, H.; Holloway, P. Efficient and Photostable ZnS-Passivated CdS:Mn Luminescent Nanocrystals. *Adv. Funct. Mater.* **2004,** *14* (2), 152-156.

32. Li, L.; Pandey, A.; Weder, D. J.; Khanal, B. P.; Pietryga, J. M.; Klimov, V. I. Efficient Synthesis of Highly Luminescent Copper Indium Sulfide-Based Core/Shell Nanocrystals with Surprisingly Long-Lived Emission. *J. Am. Chem. Soc.* **2011,** *133* (5), 1176-1179.

33. Nirmal, M.; Brus, L. Luminescence Photophysics in Semiconductor Nanocrystals. *Acc. Chem. Res.* **1999,** *32*, 407-414.

34. Gu, Z.; Zou, L.; Fang, Z.; Zhu, W.; Zhong, X. One-pot synthesis of highly luminescent CdTe/CdS core/shell nanocrystals in aqueous phase. *Nanotech.* **2008,** *19*, 135604.

35. Reiss, P.; Protiere, M.; Li, L. Core/shell semiconductor nanocrystals. *Small* **2009,** *5* (2), 154-168.

36. Li, L.; Daou, T. J.; Texier, I.; Chi, T. T. K.; Liem, N. Q.; Reiss, P. Highly Luminescent CuInS2/ZnS Core/Shell Nanocrystals: Cadmium-Free Quantum Dots for In Vivo Imaging. *Chem. Mater.* **2009,** *21* (12), 2422-2429.

37. Song, W.-S.; Yang, H. Efficient White-Light-Emitting Diodes Fabricated from Highly Fluorescent Copper Indium Sulfide Core/Shell Quantum Dots. *Chem. Mater.* **2012,** *24* (10), 1961-1967.

38. Panthani, M. G.; Khan, T. A.; Reid, D. K.; Hellebusch, D. J.; Rasch, M. R.; Maynard, J. A.; Korgel, B. A. In Vivo Whole Animal Fluorescence Imaging of a Microparticle-Based Oral Vaccine Containing (CuInSexS2-x)/ZnS Core/Shell Quantum Dots. *Nano Lett.* **2013,** *13* (9), 4294-4298.

39. Kay, A.; Grätzel, M. Dye-Sensitized Core-Shell Nanocrystals: Improved Efficiency of Mesoporous Tin Oxide Electrodes Coated with a Thin Layer of an Insulating Oxide. *Chem. Mater.* **2002,** *14* (7), 2930-2935.

40. Kim, S.; Fisher, B.; Eisler, H.-J.; Bawendi, M. Type-II Quantum Dots: CdTe/CdSe (Core/Shell) and CdSe/ZnTe (Core/Shell) Heterostructures. *J. Am. Chem. Soc.* **2003,** *125* (38), 11466-11467.

41. Panthani, M. G.; Stolle, C. J.; Reid, D. K.; Rhee, D. J.; Harvey, T. B.; Akhavan, V. A.; Yu, Y.; Korgel, B. A. CuInSe2 Quantum Dot Solar Cells with High Open-Circuit Voltage. *J. Phys. Chem. Lett.* **2013,** *4* (12), 2030-2034.

42. Cassette, E.; Pons, T.; Bouet, C.; Helle, M.; Bezdetnaya, L.; Marchal, F.; Dubertret, B. Synthesis and Characterization of Near-Infrared Cu-In-Se/ZnS Core/Shell Quantum Dots for In vivo Imaging. *Chem. Mater.* **2010,** *22* (22), 6117-6124.

43. Yarema, O.; Bozyigit, D.; Rousseau, I.; Nowack, L.; Yarema, M.; Heiss, W.; Wood, V. Highly Luminescent, Size- and Shape-Tunable Copper Indium Selenide Based Colloidal Nanocrystals. *Chem. Mater.* **2013,** *25* (18), 3753-2757.

44. Newbury, D. E.; Richie, N. W. M. Is scanning electron microscopy/energy dispersive x-ray spectrometry (SEM/EDS) quantitative? *Scanning* **2013,** *35* (3), 141-168.

Biography

Soa-Jin Catherine Sher was born in Austin, Texas in 1993 to James and Yu-Ju Sher, and graduated from John B. Connally High School as a National Merit Scholar, AP Scholar with Distinction, and valedictorian of the class of 2011. While at the University of Texas at Austin, she majored in chemical engineering and Plan II Honors, and was active in a variety of student organizations, including the Society of Asian Scientists and Engineers (SASE), Student Engineering Council (SEC), Student Engineering Educating Kids (SEEK), Tau Beta Pi (TBP), and the Society of Plan II Engineers (SP2E).

Soa-Jin began her undergraduate research experience in Dr. Arumugam Manthiram's lab, under the supervision of Dr. Matthew West, working on solid oxide fuel cell cathode materials for two years, before further exploring her interests in renewable energy and materials in Dr. Brian Korgel's lab, under the supervision of Dr. C. Jackson Stolle. She graduated Phi Beta Kappa in 2015, and will be working for BASF as a chemical engineer after graduation.